Letter

Bending immunity in valley edge states and non-Hermitian supercoupling effects

Tianyuan Liu,[1,2,3] Wei Yan,[2,3,*] and Min Qiu[2,3,4,†]

[1]*College of Information Science and Electronic Engineering, Zhejiang University, Hangzhou 310027, People's Republic of China*

[2]*Key Laboratory of 3D Micro/Nano Fabrication and Characterization of Zhejiang Province, School of Engineering, Westlake University, 18 Shilongshan Road, Hangzhou 310024, Zhejiang Province, China*

[3]*Institute of Advanced Technology, Westlake Institute for Advanced Study, 18 Shilongshan Road, Hangzhou 310024, Zhejiang Province, China*

[4]*Westlake Institute for Optoelectronics, Fuyang, Hangzhou 311421, China*

(Received 5 June 2023; revised 31 May 2024; accepted 7 June 2024; published 9 July 2024)

Breaking parity ($\mathcal{P}$) symmetry in C_6 crystals is a common routine to implement a valley topological phase. At an interface between two crystals of opposite valley Chern numbers, the so-called valley topological edge states (VTESs) emerge, and they have been proven useful for wave transport with robustness against 120° bending and a certain level of disorder. Here, we first revisit the bending-immune mechanism of VTESs by developing a lattice coupled mode theory to analyze coupling dynamics between VTESs, and further performing a perturbative analysis to estimate the Bragg scattering at the bending corner. Our analysis quantitatively evidences that the bending reflection is suppressed by the unique modal profiles of the VTESs—momentum hot spots localized at high-symmetric K (K') points—which only concerns the existence of the valleys in the bulk band diagrams, and imposes no requirement on topology. Second, we reveal the emergence of *non-Hermitian supercoupling* (SC) effects in (Hermitian) valley systems: Counterflow, momentum-matched incident and transmission ESs could reach ∼100% coupling efficiency free of corner reflection and construct an unusual *superexponential* field distribution. Based on two findings, a coherent understanding of bending immunity for ESs in valley systems is established, and different designs based on rhombic lattices are proposed. Additionally, we demonstrate that the emerged superexponential field profile due to the SC effects provides another way to engineer the photonic Purcell factor.

DOI: 10.1103/PhysRevB.110.L020101

Introduction. Recently, topology, a mathematical concept of classification, has spawned a new perspective in physics [1,2]. When two insulators of different topological invariants are interfaced, gapless edge states (ESs) emerge, enabling transport robustness [3,4]. Various approaches have been proposed to realize topological phases, including breaking time reversal symmetry, utilizing spin or valley degrees of freedom, and so on [5–11].

Recently, valley topology (VT) has been widely implemented in photonics due to its combination of topological superiority and fabrication feasibility [11], even though the valley Chern number is not an exact topological invariant [12–14]. Taking a C_6-symmetric hexagonal lattice for example, by slightly modifying A and B sublattices, one breaks inversion symmetry and generates opposite Berry curvatures at the K and K' valleys [Fig. 1(a)]. This leads to valley Chern numbers $C_v \sim \pm 1/2$ [15]. When two photonic crystals (PhCs) with opposite C_v's are interfaced along zigzag terminations, VTESs emerge, the hallmark of which is the ability to transport through 120° bending [11] and against random disorders [16,17]. These merits facilitate a variety of applications, including topological lasers [18], slow light waveguides [19,20], and high-fidelity transmission lines [17,21].

Though the achievements in VT photonics are evident, the common perspective which attributes their merits to topological protection is rather ambiguous. Figure 1 demonstrates that when VT PhCs are continuously deformed into a trivial case where VT protection no longer exists, the ESs remain bending immune. The exemplified deformation includes two parts, quantified by the detuning ratio of the radii of silicon rods, $D \equiv (r_A - r_B)/r_B$. First, D increases from 0 to 1 [Fig. 1(b)], an evolution from the VT to VT-trivial phase (that is, PhCs regain inversion symmetry and the C_v's become zero). Second, the sublattice B is rebuilt [Fig. 1(c)], so that both PhCs possess the same C_v's (suggesting that the ESs can no longer be classified as VTESs). In the whole procedure, a 100% transmittance passband through a Z-shaped bending exists and coincides with the ES bandwidth [Fig. 1(d)]. Moreover, no qualitative difference is observed in the resilience to random disorders in these cases (see Supplemental Material Fig. S6 [22]). It is thus necessary to look into the *real origin* of these properties which were commonly attributed to VT protection. This topic is also relevant to and intensified by a few recent experiments that observe a similar resilience to sharp bending and fabrication errors in PhCs with and without VT protection [23,24].

Strategy. We revisit the propagation of VTESs through a 120° bend. As sketched in Fig. 2(a), it is a two-step process. First, as an incident ES propagates towards the bending corner, it couples to the reflection, transmission, and "inverse"-transmission ESs due to modal overlapping. Second, after propagating through the coupling region, a

*Contact author: wyanzju@gmail.com
†Contact author: qiumin@westlake.edu.cn

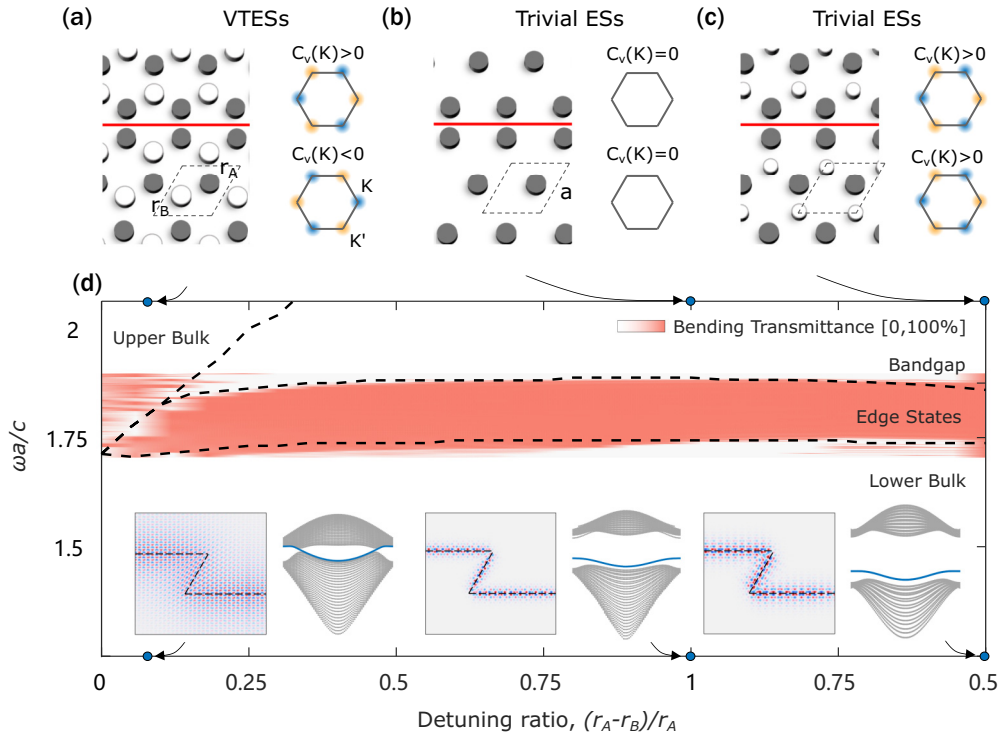

FIG. 1. Evolution of photonic ESs and their bending-immune ability during a deformation procedure where VT protection is gradually broken. The deformation starts with a standard VT case (a). Then, the radius of rod B is reduced until elimination where both side PhCs become VT trivial (b). Finally, rod B is rebuilt so that both side PhCs possess the same VT phase (c). (d) During the whole procedure, a 100% transmittance passband through a Z-shaped bend is always present. Transverse electric (TE) polarized light with the electric field in the out-of-plane direction [25] is considered.

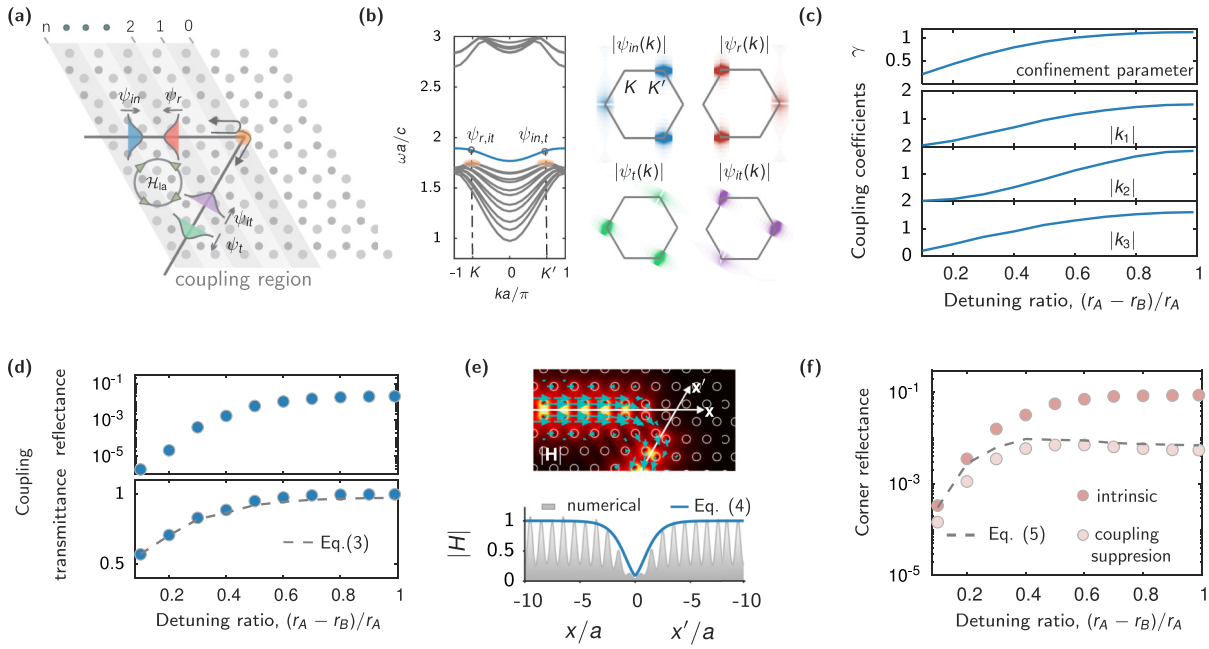

FIG. 2. Bending-immune mechanism. (a) Sketch of an ES propagating through a 120° bend. (b) Projected band diagram for a ribbon composed of two interfaced hexagonal PhCs (left panel), and momentum profiles of ESs (right panel). The PhC uses the same material and geometrical compositions as Fig. 1 with $D = 1$ (radii detuning ratio), and light is TE polarized. (c) Confinement parameter and coupling coefficients as functions of D, corresponding to a continuous evolution from the VT to VT-trivial phase. (d) Coupling reflectance and transmittance (markers) by solving Eq. (1). (e) Magnetic field magnitude (color map) and power flow (arrows) for an ES propagating through a 120° bend with $D = 1$. The lower panel plots the field profile along the bending edges. (f) Corner reflectance, contrasting the results including (bright markers) and excluding (dark markers) the non-Hermitian coupling effect.

fraction of the incident ES reaches the corner, and hits upon a semi-infinite PhC. In both processes, reflections could be induced through evanescent coupling and Bragg scattering, respectively, these are analyzed below.

Lattice CMT. In the first process, coupling between ESs exhibits two features: (1) nonuniformity in space due to PhC periodicity, and (2) strength increasing as ESs approach the corner. To capture these features, we employ the Lorentz reciprocity theorem and derive a lattice coupled mode theory (CMT) (see derivations in Supplemental Material Note 1 [22]) [26],

$$-i\mathcal{P}(|\boldsymbol{\psi}^{n+1}\rangle - |\boldsymbol{\psi}^{n}\rangle) = \mathcal{H}^{n}_{\mathrm{la}}(|\boldsymbol{\psi}^{n+1}\rangle + |\boldsymbol{\psi}^{n}\rangle)/2, \qquad (1)$$

where $|\boldsymbol{\psi}^{n}\rangle \equiv [a^{n}_{in}; a^{n}_{t}; a^{n}_{r}; a^{n}_{it}]$ $(n = 0, 1, \ldots)$ are the ES amplitudes at the nth cutting line of the PhCs in the coupling region [Fig. 2(a)], $|a^{n}_{in,t,r,it}|^2$ represent the ES power; $\mathcal{P} = \mathrm{diag}[1; -1; -1; 1]$ with $\mathcal{P}_{ii} = 1, -1$ meaning that the ESs propagate towards and outwards from the corner, respectively; and $\mathcal{H}^{n}_{\mathrm{la}}$ is the coupling-coefficient matrix.

$\mathcal{H}^{n}_{\mathrm{la}}$ relates to the modal profiles. Consider the incident ESs in Fig. 1 with the wave number equal to the projected valley K' point. The incident and transmission ESs are identified to have momentum hot spots at the K' point, while the reflection and inverse-transmission ESs have momentum hot spots at the K point, as shown in Fig. 2(b) for a VT-trivial phase (with detuning ratio $D = 1$) and in Supplemental Material Fig. S4 for more results [27]. This momentum characteristic is present throughout the numerical examples independent of topology. It is simply because that the bulk Bloch modes, spectrally closest to these ESs, are those at the K and K' valley points [see the left panel in Fig. 2(b)]. Accordingly, the decomposition of the ESs into the bulk Bloch modes should mainly consist of the bulk valley modes, thus leading to K/K' momentum localizations (see more discussions in Supplemental Material Note 5 [22]). In the real space, the ESs are localized around the edges with the lateral $1/e$ confinement length denoted by $1/\alpha$ (α, decay wave number). These modal features render $\mathcal{H}^{n}_{\mathrm{la}}$ as a specific form,

$$\mathcal{H}^{n}_{\mathrm{la}} = \begin{bmatrix} 0 & k_1 e^{-n\gamma} & k_2 e^{-2n\gamma+i\phi} & k_3 e^{-n\gamma-i\phi/2} \\ k_1^* e^{-n\gamma} & 0 & k_3^* e^{-n\gamma+i\phi/2} & k_2^* e^{-2n\gamma-i\phi} \\ k_2^* e^{-2n\gamma-i\phi} & k_3^* e^{-n\gamma+i\phi/2} & 0 & k_1^* e^{-n\gamma} \\ k_3 e^{-n\gamma-i\phi/2} & k_2 e^{-2n\gamma+i\phi} & k_1 e^{-n\gamma} & 0 \end{bmatrix}, \qquad (2)$$

with phase parameter $\phi = 4\pi/3, -4\pi/3$ for the wave number of the incident ESs equal to the projected K and K' points, respectively, and the confinement parameter $\gamma = \alpha a\sqrt{3}/2$ (a, lattice constant). The coupling coefficients k_i $(i = 1, 2, 3)$ are given as overlap integrals of normalized ESs (see Supplemental Note 1 for derivations and Supplemental Material Fig. S8 for numerical demonstrations [22]). Note that the momentum matching between incident (reflection) and transmission (inverse-transmission) ESs results in a constant phase of the associated coupling coefficients independent of propagation index n.

Non-Hermitian coupling. The lattice CMT is employed to examine the coupling dynamics between ESs. To this end, we define the coupling transmittance (T_{couple}), reflectance (R_{couple}) as ratios of the coupled-out power of the transmission, and reflection ESs to the incident power, respectively. Figure 2(d) plots T_{couple} and R_{couple} for the evolution from the VT to VT-trivial phase (cf. Fig. 1). It shows that T_{couple} is two to three orders of magnitude larger than R_{couple}. Notably, T_{couple} almost approaches 1 as $D \to 1$, with the increasing of the coupling strength [cf. Fig. 2(c)]. The efficient incident-transmission coupling has an intuitive interpretation. The coupling coefficients between the incident and transmission ESs keep the same phase independent of propagation index n due to their matched momenta, which facilitates the accumulation of the transmission power. Conversely, the phase variation in the coupling coefficients between the incident and reflection ESs inhibits the accumulation of the reflection power.

To gain deeper insights beyond the intuitive momentum-matching picture, we perform an analytic analysis by retaining the dominant incident and transmission components in Eq. (1), and taking the continuum limit. The lattice CMT equation is then cast in the form of Schrödinger's equation $-id|\boldsymbol{\psi}(\ell)\rangle/d\ell = \mathcal{H}_c(\ell)|\boldsymbol{\psi}(\ell)\rangle$, characterizing the incident-transmission coupling. Here, ℓ is the distance to the corner, $|\boldsymbol{\psi}(\ell)\rangle \equiv [a_{\mathrm{in}}(\ell); a_t(\ell)]$, and $\mathcal{H}_c(\ell) = [0, k_1 e^{-\gamma\ell/a+\gamma/2}/a; -k_1^* e^{-\gamma\ell/a+\gamma/2}/a, 0]$. Interestingly, despite its origin in the Hermitian system, $\mathcal{H}_c$ is *non-Hermitian*. The non-Hermiticity leads to that $|a_{\mathrm{in}}(\ell)|^2 + |a_t(\ell)|^2$ is not a conserved quantity. This does not contradict with the energy conservation, since the total power of the incident and transmission edge states is $|a_{\mathrm{in}}(\ell)|^2 - |a_t(\ell)|^2$ (the minus sign is due to that the power flow of incident and transmission ESs are opposite, i.e., toward and outward corner, respectively), which is conserved. Therefore, it is apparent that the coupling non-Hermiticity is not due to material/radiation loss or gain, but rather emerges from the transmission and reflection ESs that carry the counterpropagating power flow.

Moreover, it is worth noting that the eigenvalues of $\mathcal{H}_c$ are pure imaginary numbers, which is due to the non-Hermiticity, and also the momentum matching of incident and transmission ESs that makes the diagonal components of the $\mathcal{H}_c$ vanish. As a result, the conventional Hermitian coupling phenomena, such as mode beating and energy hopping back and forth between coupled channels [26], which rely on the real eigenvalues of the coupling Hamiltonian, disappear. It unexpectedly brings efficient incident-transmission coupling in the present valley system. Specifically, T_{couple} is derived by expanding $|\boldsymbol{\psi}(\ell)\rangle$ with the eigenstates of $\mathcal{H}_c$ (see Supplemental Material Note 2 [22]):

$$T_{\mathrm{couple}} = \tanh^2(k_{\mathrm{sc}}) \quad \text{with} \quad k_{\mathrm{sc}} = |k_1| e^{\gamma/2}/\gamma. \qquad (3)$$

The non-Hermitian trait is evident: T_{couple} increases monotonically with the coupling parameter k_{sc}, which is absent in the Hermitian scenario, where the mode beating inevitably gives rise to periodic variations of T_{couple} as the coupling parameter varies. Consequently, as long as $k_{\text{sc}} \gg 1$, T_{coupling} is destined to approach 1 [Fig. 2(d)]. As shown in the lower panel of Fig. 2(d), the prediction of Eq. (3) (dashed line) agrees well with the numerical solution.

Furthermore, the non-Hermitian coupling, with the exponential growth of its strength as ℓ decreases [Eq. (2)], result in an unusual *superexponential* field distribution of the ESs (see Supplemental Material Note 2 for derivations [22]),

$$|a_{\text{in},t}(\ell)| = \exp\left[-k_{\text{sc}} \exp(-\gamma \ell/a)\right]. \tag{4}$$

The superexponential distribution is verified in Fig. 2(e), which plots the field distribution for an ES propagating through a 120° bend with $D = 1$. The upper panel shows that the field rapidly decays when approaching the corner, and the power flow makes a smooth U-turn to the transmission channel. The lower panel plots the field profile along the bending edges, showing agreement between the numerical (shadow area) and analytic [solid line, Eq. (4)] results. More numerical results that verify the predictive accuracy of Eq. (4) are provided in Supplemental Material Fig. S9 [22].

The superexponential profile also benefits the bending immunity of ESs. Specifically, the coupling coefficients related to reflection ES grow exponentially when approaching the corner [see Eq. (2)]. Nevertheless, the faster superexponential decay of the field overshadows this exponentially growing coupling term, thus reducing the coupling to the reflection channel.

Corner reflectance. After the non-Hermitian coupling process, a fraction of the incident ES arrives at the corner, and then induces the transmission and reflection ESs through Bragg scattering by a semi-infinite PhC [Fig. 2(a)]. In a Bragg scattering event, efficient excitation of a wave requires its momentum matching with the diffracted momentum of the incident one. The transmission ES fulfills this condition, since its momentum distributions coincide with those of the incident ES, while the reflection ES does not. As a result, the corner reflectance is expected to be negligible. To put it in concrete terms, we evaluate the power ratio of the corner-scattered reflection ES to the transmission ESs by comparing the overlap integrals between the incident and the transmission/reflection ESs in the scattering region. Meanwhile, recall that the incident ES at the corner is reduced by a factor $e^{-k_{\text{sc}}}$ [Eq. (4)] due to the efficient non-Hermitian coupling. Taking these factors into account, the corner reflectance R_{cn} is estimated to be about (see Supplemental Material Note 3 for derivations [22])

$$R_{cn} \sim e^{-2k_{\text{sc}}} \frac{(1-e^{-\gamma})^2(1-e^{-2\gamma})^2}{3|1-e^{i\phi-2\gamma}|^2}. \tag{5}$$

Figure 2(f) plots the corner reflectance (bright markers) simulated with COMSOL MULTIPHYSICS. The corner reflectance is observed to be negligible, and its magnitude agrees with Eq. (5) (dashed line). Additionally, to better visualize the role of the non-Hermitian coupling in reducing the corner reflection, the *intrinsic* corner reflectance is also plotted (dark markers) by dividing simulated R_{cn} with the coupling factor $e^{-2k_{\text{sc}}}$. It demonstrates that the coupling effect noticeably suppresses the corner reflection.

We thus evidence, the momentum matching between the incident and transmission ESs due to their coinciding momenta around the K/K' points, brings about the bending immunity of the edge states by enabling efficient non-Hermitian incident-transmission coupling and suppressing the corner reflection. Our theoretical observation also well explains the recently reported experimental results of Dai *et al.* [28], which evidence that the bending immunity of the edge states in the valley system is not protected by topology (see Supplemental Material Note 6 for detailed discussions [22]).

Supercoupling effects. As discussed above, the non-Hermitian coupling between the incident and transmission ESs can be efficient, leading to ∼100% coupling transmittance and superexponential field distribution. These interesting physical consequences are termed *supercoupling (SC) effects* for the convenience of discussion. The realization of efficient SC effects requires three elements concerning the incident and transmission ESs: (1) counterflow power, (2) momentum matching, and (3) strong coupling ($k_{\text{sc}} \gg 1$). The first two elements bring the non-Hermitian coupling that suppresses the mode beating, while the last one is essential for high efficiency. None of them demands topology, thus implying the possibility of the realization in more general platforms. Below, such a demonstration is given using rhombic PhCs.

The left panel of Fig. 3(a) sketches a bend constructed by two interfaced rhombic PhCs made of periodic silicon rods in air. The acute interior angle of the rhombic lattice is denoted by θ_{rh} (note that when $\theta_{\text{rh}} = 60°$, the lattice becomes a hexagon). The right panel of Fig. 3(a) plots the projected band diagram (TE polarization) for a ribbon composed of interfaced rhombic PhCs with $\theta_{\text{rh}} = 45°$ and $r_A = 0.12a$ (rod radius). Similar to the hexagonal case, an ES band emerges above a bulk band. The bulk band exhibits valleys (marked with shadow ellipses), which, however, are slightly located away from the vertices of the reciprocal Wigner-Seitz (WS) cell (e.g., O and N points), due to symmetry reduction. Consequently, for an ES with a wave number equal to the projected O/N point, their momentum hot spots are slightly away from the vertices of the WS cell [see the insets in Fig. 3(a)]. Nevertheless, the momentum profiles of the incident and transmission ESs still maintain a large overlap.

The upper panel of Fig. 3(b) plots the coupling parameter k_{sc} vs θ_{rh}. Here, θ_{rh} varies from 45° to 70°, within which the ESs of interest propagate in a single-mode fashion. It shows that k_{sc} increases as θ_{rh} decreases. This increment is attributed to the slow-light effect, with which the coupling coefficient increases proportionally to the group refractive index n_g of the ES (an explicit relation between k_{sc} and n_g is given in Supplemental Material Note 4 [22]); n_g is also plotted, whose evolution is well consistent with k_{sc}. This thus suggests the enhancement of the SC effects by the slow-light effect. For instance, when $\theta_{\text{rh}} = 45°$, n_g is one order of magnitude larger than at $\theta_{\text{rh}} = 60°$, resulting in the growth of k_{sc} (that measures the SC effects) by the same order.

The enhanced SC effects are visualized in Fig. 3(c) that plots the field distribution for an ES propagating through the bend with $\theta_{\text{rh}} = 45°$. The wave number of the incident

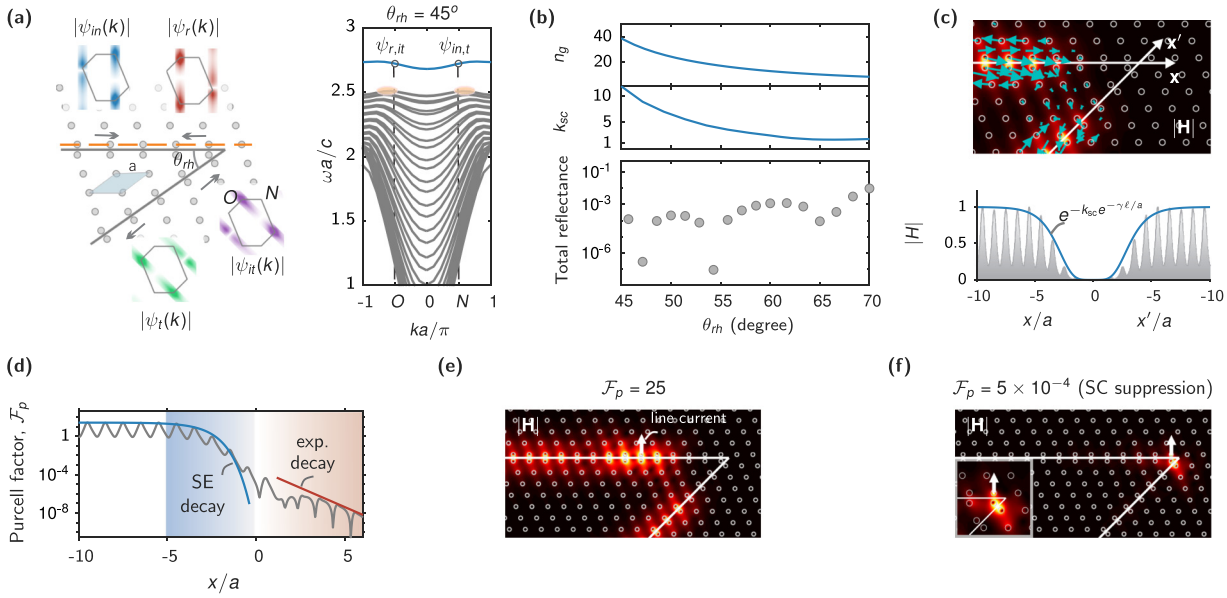

FIG. 3. Enhanced supercoupling effects by leveraging the slow-light effect in rhombic PhCs. (a) Sketch of a bend composed of two interfaced rhombic PhCs (left panel), and projected band diagram for a ribbon structure with rhombic angle $\theta_{\rm rh} = 45^\circ$. Insets: Momentum profiles of ESs with wave number of incident ES equal to the projected N point. Light is TE polarized. (b) Coupling parameter $k_{\rm sc}$, group refractive index n_g of ESs (upper panel), and bend reflectance (lower panel) vs rhombic angle. (c) Magnetic field magnitude (color map) and power flow (arrows) for an ES propagating through a bend with $\theta_{\rm rh} = 45^\circ$. The lower panel plots the field profile along the bending edges. (d) Purcell factor for a line current along a horizontal cutting line nearby the incident edge [red dashed line in (a)] with $\theta_{\rm rh} = 45^\circ$. (e) and (f) Magnetic field distributions for a line current placed far away from and close to the corner, respectively (marked with arrows). The rhombic PhC is composed of Si rods (radius, $r_A = 0.12a$) in air.

ES is equal to the projected N point [Fig. 3(a)]. The upper panel shows that the incident ES is fully coupled to the transmission ES at a few lattice distances to the corner, thus making the field completely vanish around the corner region. The lower panel confirms that the superexponential profile, Eq. (4), accurately characterizes the field distribution along the bending edges. The efficient coupling between the incident and transmission ESs overshadows the induction of the reflection ES, and results in a bending immunity of the edge states with negligible reflectance [see the lower panel in Fig. 3(b)].

The superexponential distribution characterizes the rapid decay of the ES towards the corner. Based on the reciprocal principle, it also suggests that, if a quantum emitter is placed near the corner, its radiation should be heavily suppressed despite the presence of available ES channels. The principle is different from the conventional strategy based on the band-gap effect of PhCs. It is alternatively due to the emitted outgoing ESs being efficiently coupled to the ingoing ESs through the non-Hermitian coupling, making power circulate within the corner and hard to escape. To quantify this radiation suppression, we compute the Purcell factor $\mathcal{F}_p$ for a line current (in a direction perpendicular to the page) along a horizontal cutting line close to the incident edge [red dashed line in Fig. 3(a)]. As is shown in Fig. 3(d), $\mathcal{F}_p$ superexponentially decays by more than four orders of magnitude within a few lattice distances when the position of the line current approaches the corner. After crossing the corner, the rapid superexponential decay turns to a mild exponential decay due to the band-gap effect. Figures 3(e) and 3(f) plot the field distributions for the line current placed far away from and close to the corner, respectively, verifying that the supercoupling effects efficiently inhibit the radiation.

Summary. First, based on the lattice coupled mode theory and perturbative analysis, we clearly identify the critical role of momentum matching between incident and transmission ESs (due to their coinciding momentum hot spots around the high-symmetric K/K' points) in supporting the bending immunity of the VTESs. Second, we reveal the non-Hermitian coupling between the incident and transmission ESs in valley systems, which leads to the supercoupling (SC) effects, featuring efficient incident-transmission coupling and a superexponential field distribution. With these insights, one can realize bending-immune transport free of the topology constraint such as using C_3 or rhombic PhCs with a topology-trivial phase, and potentially propose other designs that follow the same principle (see Supplemental Material Fig. S10 for additional numerical results on bending-immune edge states [22]), and utilize the SC effects to manipulate light-matter interactions.

[1] T. Ozawa, H. M. Price, A. Amo, N. Goldman, M. Hafezi, L. Lu, M. C. Rechtsman, D. Schuster, J. Simon, O. Zilberberg, and I. Carusotto, Topological photonics, Rev. Mod. Phys. **91**, 015006 (2019).

[2] X.-L. Qi and S.-C. Zhang, Topological insulators and superconductors, Rev. Mod. Phys. **83**, 1057 (2011).
[3] L. Lu, J. D. Joannopoulos, and M. Soljačić, Topological photon, Nat. Photon. **8**, 821 (2014).
[4] F. D. M. Haldane and S. Raghu, Possible realization of directional optical waveguides in photonic crystals with broken time-reversal symmetry, Phys. Rev. Lett. **100**, 013904 (2008).
[5] Z. Wang, Y. D. Chong, J. D. Joannopoulos, and M. Soljačić, Reflection-free one-way edge modes in a gyromagnetic photonic crystal, Phys. Rev. Lett. **100**, 013905 (2008).
[6] Z. Wang, Y. Chong, J. D. Joannopoulos, and M. Soljačić, Observation of unidirectional backscattering-immune topological electromagnetic states, Nature (London) **461**, 772 (2009).
[7] M. Hafezi, E. A. Demler, M. D. Lukin, and J. M. Taylor, Robust optical delay lines with topological protection, Nat. Phys. **7**, 907 (2011).
[8] M. C. Rechtsman, J. M. Zeuner, Y. Plotnik, Y. Lumer, D. Podolsky, F. Dreisow, S. Nolte, M. Segev, and A. Szameit, Photonic Floquet topological insulators, Nature (London) **496**, 196 (2013).
[9] A. B. Khanikaev and G. Shvets, Two-dimensional topological photonics, Nat. Photonics **11**, 763 (2017).
[10] T. Ma and G. Shvets, All-Si valley-Hall photonic topological insulator, New J. Phys. **18**, 025012 (2016).
[11] H. Xue, Y. Yang, and B. Zhang, Topological valley photonics: physics and device applications, Adv. Photonics Res. **2**, 2100013 (2021).
[12] A. Alexandradinata, J. Höller, C. Wang, H. Cheng, and L. Lu, Crystallographic splitting theorem for band representations and fragile topological photonic crystals, Phys. Rev. B **102**, 115117 (2020).
[13] M. Proctor, P. A. Huidobro, B. Bradlyn, M. B. de Paz, M. G. Vergniory, D. Bercioux, and A. García-Etxarri, Robustness of topological corner modes in photonic crystals, Phys. Rev. Res. **2**, 042038(R) (2020).
[14] S. Wong, M. Saba, O. Hess, and S. S. Oh, Gapless unidirectional photonic transport using all-dielectric kagome lattices, Phys. Rev. Res. **2**, 012011(R) (2020).
[15] D. Xiao, M.-C. Chang, and Q. Niu, Berry phase effects on electronic properties, Rev. Mod. Phys. **82**, 1959 (2010).
[16] G. Arregui, J. Gomis-Bresco, C. M. Sotomayor-Torres, and P. D. Garcia, Quantifying the robustness of topological slow light, Phys. Rev. Lett. **126**, 027403 (2021).
[17] X.-T. He, E.-T. Liang, J.-J. Yuan, H.-Y. Qiu, X.-D. Chen, F.-L. Zhao, and J.-W. Dong, A silicon-on-insulator slab for topological valley transport, Nat. Commun. **10**, 872 (2019).
[18] Y. Zeng, U. Chattopadhyay, B. Zhu, B. Qiang, J. Li, Y. Jin, L. Li, A. G. Davies, E. H. Linfield, B. Zhang, Y. Chong, and Q. J. Wang, Electrically pumped topological laser with valley edge modes, Nature (London) **578**, 246 (2020).
[19] H. Yoshimi, T. Yamaguchi, Y. Ota, Y. Arakawa, and S. Iwamoto, Slow light waveguides in topological valley photonic crystals, Opt. Lett. **45**, 2648 (2020).
[20] H. Yoshimi, T. Yamaguchi, R. Katsumi, Y. Ota, Y. Arakawa, and S. Iwamoto, Experimental demonstration of topological slow light waveguides in valley photonic crystals, Opt. Express **29**, 13441 (2021).
[21] Y. Yang, Y. Yamagami, X. Yu, P. Pitchappa, J. Webber, B. Zhang, M. Fujita, T. Nagatsuma, and R. Singh, Terahertz topological photonics for on-chip communication, Nat. Photon. **14**, 446 (2020).
[22] See Supplemental Material at http://link.aps.org/supplemental/10.1103/PhysRevB.110.L020101 for derivations of lattice coupled mode theory derivations of non-Hermitian supercoupling effects; derivations of corner reflectance; relationship between coupling coefficients and group velocity of edge states; discussions on modal expansion of edge states; dicussions on bending-immune experiments reported in Ref. [28]; and supplemental numerical results, which includes Refs. [16,26,28,29].
[23] C. A. Rosiek, G. Arregui, A. Vladimirova, M. Albrechtsen, B. Vosoughi Lahijani, R. E. Christiansen, and S. Stobbe, Observation of strong backscattering in valley-Hall photonic topological interface modes, Nat. Photon. **17**, 386 (2023).
[24] W. Dai, T. Yoda, Y. Moritake, M. Ono, E. Kuramochi, and M. Notomi, Origin of high transmission in 120-degree sharp bends of photonic-crystal waveguides with and without inversion symmetry, in *Conference on Lasers and Electro-Optics* (Optica Publishing Group, Washington, DC, 2022), p. FW1C.1.
[25] J. Kong, *Electromagnetic Wave Theory* (EMW Publishing, Cambridge, MA, 2005).
[26] H. Haus, W. Huang, S. Kawakami, and N. Whitaker, Coupled-mode theory of optical waveguides, J. Lightwave Technol. **5**, 16 (1987).
[27] X. Wu, Y. Meng, J. Tian, Y. Huang, H. Xiang, D. Han, and W. Wen, Direct observation of valley-polarized topological edge states in designer surface plasmon crystals, Nat. Commun. **8**, 29101323 (2017).
[28] W. Dai, T. Yoda, Y. Moritake, M. Ono, E. Kuramochi, and M. Notomi, High transmission in 120-degree sharp bends of inversion-symmetric and inversion-asymmetric photonic crystal waveguides, arXiv:2310.17487.
[29] J. Yang, J.-P. Hugonin, and P. Lalanne, Near-to-far field transformations for radiative and guided waves, ACS Photonics **3**, 395 (2016).